A Chimera method to generate realistic vortices and to model their interaction with airfoils

Christoph Wolf,* Tobias Knopp†and Dieter Schwamborn‡

DLR, German Aerospace Center, 37073 Göttingen, Germany

Abstract

A Chimera technique for moving grids is applied to simulate the generation and transport of a realistic large-scale vortex convected by a mean velocity field and to model its interaction with an airfoil. The Chimera approach allows to resolve the vortex on fine local Chimera grids, whereas the structured background grid covering most of the computational domain can be relatively coarse. While minimising the numerical costs, this approach allows to preserve the vortex throughout the complete simulation. One aim is to study the effects when varying the underlying turbulence model and the distance that the vortex is transported. Another goal is to determine, whether stall occurs due to the vortex-airfoil interaction. Indeed the main objective of this publication is to demonstrate the practical applicability of the Chimera technique for the simulation of large-scale disturbances in the onflow conditions.

1 Introduction

The modeling and simulation of large-scale vortices in the onflow conditions and their interaction with airplanes pose an immense challenge in today's air traffic. Such vortices – whose length scales range from microscopically small up to to several magnitudes of an airplane – can evolve naturally in the atmosphere due to certain weather conditions. Another source for the creation of dangerous disturbances lies in the airplanes themselves: During take–off and landing huge co-rotating wake vortices evolve [1]. The problem of wake vortices has been widely adressed in literature. In [2] a probabilistic wake-vortex model is presented. The effects of two interacting and finally merging wake vortices is illustrated in [3]. Both types of disturbances pose a great danger for oncoming airplanes and can cause fatal accidents. The status quo of avoiding the risks of wake vortices lies in waiting several minutes (depending on the size of the planes and other factors) before allowing the next airplane to take-off or land on the same runway. In times of worldwide increasing air traffic, this limitation becomes more and more problematic.

---

*Research Scientist, Institute of Aerodynamics and Flow Technology, Department $C^2A^2S^2E$, christoph.wolf@dlr.de

†Research Scientist, Institute of Aerodynamics and Flow Technology, Department $C^2A^2S^2E$

‡Head of Department, Institute of Aerodynamics and Flow Technology, Department $C^2A^2S^2E$

The focus in this publication lies on the development and application of a numerical technique that enables firstly to generate a realistic vortex, secondly to transport it towards an airfoil and thirdly to simulate the vortex-airfoil interaction in order to predict the forces and moments acting on the wing. To the knowledge of the authors no paper presenting such a technique has been published in the context of large-scale disturbances in the onflow conditions yet. First investigations concerning a vortex-airfoil interaction are presented in [4], where the collision of a single sinusoidal gust and a NACA 0012 airfoil has been examined numerically in 2D. As this simulation requires a globally fine grid, the extension to a complex 3D-configuration seems hard to achieve.

We propose the following approach, which makes use of the so-called Chimera technique [5, 6] and is illustrated in Fig. 1 - 3. Figure 1 shows the initial setting at the beginning of the computation. Embedded within a background grid ("orange") lie a "vortex generation grid" ("red") containing an airfoil to generate the vortex, a "vortex transport grid" ("green") to preserve and tranport the vortex and a "vortex interaction grid" ("blue") containing an airfoil that in the end interacts with the vortex. While the three local grids should be chosen sufficiently fine to preserve the vortex, the background grid covering most of the computational domain can be relatively coarse, thus minimising the numerical costs. First the vortex generation grid is flapped upwards relative to the background grid, see Fig. 2. As a result, the realistic vortex evolves from the trailing edge of the airfoil and moves with the free stream velocity onto the vortex transport grid. Having been interpolated onto the latter, both the vortex and the vortex transport grid are moved simultaneously with the free stream velocity towards the vortex interaction grid. As the vortex transport grid and the airfoil of the vortex interaction grid must not overlap, the vortex transport grid is stopped sufficiently far away from the airfoil, see Fig. 3. The vortex continues to move to the right and is finally interpolated onto the vortex interaction grid, where the vortex-airfoil interaction eventually takes place.

2 Numerical method

2.1 The DLR TAU Code

The DLR TAU Code [7] is a finite volume computational fluid dynamics solver for the three-dimensional compressible RANS equations in integral form. As all flow variables are stored at the cell vertices (or respectively at the cell centers with respect to the dual grid cells) the code is independent of the type of grid cells, which allows the use of unstructured, structured or hybrid grids. For the discretization of the convective fluxes, several upwind, central or mixed upwind-central discretization methods are available. The present computations are performed by a second–order accurate central differencing scheme with artifical matrix dissipation [8] using standard settings. The gradients of the flow variables are determined by a Least Square formula. The time-accurate simulations are performed using dual-time. Within each time step the nonlinear problem is solved in pseudo time using an implicit LUSGS scheme [9]. For convergence acceleration residual smoothing and multigrid methods have been used.

2.2 The Chimera technique

The Chimera technique [10, 11] allows flow solutions on overlapping grids, where the grids can be in relative motion to each other during a simulation. To illustrate the principle of the Chimera technique it is sufficient to study the case of a cartesian vortex grid lying embedded

within a cartesian background grid. Those points of the background grid that are located in the interior of the vortex grid have to be blanked out (this procedure is commonly referred to as "hole-cutting"). This is achieved by using a hole definition grid, which is placed in the interior of the vortex grid. A hole definition grid usually is a simple polygonal domain and should be chosen significantly smaller than the vortex grid. This ensures a sufficiently large overlapping region of the vortex grid and the active part of the background grid. Figure 4 (left) shows a cartesian vortex grid (solid blue lines) placed within a cartesian background grid (dashed red lines). Also the boundary of the small hole definition grid (solid black lines) can be seen. Next a variable "iblank" is assigned to each grid point of both the vortex grid and the background grid, where possible values of iblank are 0, 1 or 2. Points of the background grid that lie in the region covered by the hole definition grid and therefore are excluded from the computation are marked by 0. How these points can be identified efficiently is described in [12]. An iblank–value of 1 indicates that the numerical computation at this point can be performed normally. A grid point with an iblank–value of 2 is either located in the outer boundary of the vortex grid or in the inner artificial boundary around the hole of the background grid. The flow data for these points are obtained by interpolation from the respectively other grid. Figure 4 (right) shows all grid points containing an iblank value of 0 or 2 (the points with a value of 1 are omitted for better visibility). In the inner block, which is made up of points of the background grid, the hole consisting of 9 points (iblank–value 0) is surrounded by the points of the inner boundary of the background grid (iblank-value 2). The points in the outer frame (iblank-value 2) belong to the outer boundary of the vortex grid. As the interpolation of the numerical fluxes leads to problems [13], the conservative variables are used instead. The accuracy of the interpolation is prescribed as bilinear (for a 2D–computation), as this is sufficient for maintaining the second order accuracy in space of the numerical scheme [14]. The task of finding appropriate donor grid points, from which the data can be obtained for interpolation, is discussed in detail in [10, 15]. Having performed the interpolation and computation within a physical time step, both the vortex grid and the hole definition grid can then be moved simultaneously relative to the background grid and the complete procedure is performed again.

3   Results

In this section 2D-URANS computations to simulate the interaction of a realistic vortex with a two-element airfoil near stall are presented.

The principle of the technique has already been explained in section 1. While the airfoil of the vortex generation grid is a NACA 0021 airfoil, the vortex interaction grid contains an FNG ("Flügel neuer Generation"–"new generation wing") two-element airfoil.

Both a small and a large airfoil-to-airfoil distance (defined as distance between the trailing edge of the NACA 0021 airfoil and the leading edge of the FNG airfoil) of 2m and alternatively 4m has been used. While the initial relative positions of the Chimera grids in the case of the small airfoil-to-airfoil distance are identical to the situation shown in Fig. 1, the vortex interaction grid is shifted another 2m to right when using the large airfoil-to-airfoil distance (not shown). As additionally both the SAO turbulence model and the Menter-SST turbulence model have been applied, an overall of four computations have been performed.

In Fig. 5 and Fig. 6 2D-cutouts of the four Chimera grids are shown. For better comparison of the varying grid refinements, all cutouts are of an equal size of $0.4m \times 0.4m$. The vortex generation grid (containing 33000 grid points) and the vortex interaction grid (45000 points) cover a circular area of radius 0.5m and respectively 0.6m and are of hybrid type. The two

airfoils are positioned in the center of their relative grid, where the NACA 0021 airfoil has a chord length of 0.3m and the FNG airfoil one of 0.6m. (The chord length of the FNG airfoil corresponds to cruise configuration, whereas here take-off configuration is considered. Therefore the actual length of the FNG airfoil is larger than its chord length.) While the quadratic vortex transport grid ($151^2 \approx 23000$ points) of size $1m \times 1m$ looks relatively coarse in comparison, it is considered fine enough to conserve the vortex, because the grid is equidistant and cartesian, which minimes the numerical dissipation, and the transport distances are relatively short. The three Chimera grids lie embedded in the coarse background grid representing a wind tunnel (12000 points), which is also equidistant and cartesian and covers an area of $1.3m \times 6m$. Overall a 2D-plane containing all four Chimera grids contains 114000 grid points.

The origin of the x-z coordinates is set at the lower left background grid corner. At the beginning of all simulations the left boundary of the vortex generation grid of radius 0.5m is located at an x-position of 0.25m and the lower one at a z-position of 0.15m, where originally $\alpha = 0°$ is chosen at the NACA 0021 airfoil. The left boundary of the quadratic vortex transport grid of size 1m is located at x=1m, while the lower boundary is situated at z=0.15m. Based on $\alpha = 0°$ the lower boundary of the vortex interaction grid is situated at z=0.05m in all simulations, while the left boundary is located at x=2.55m in the case of the small airfoil-to-airfoil distance and at x=4.55m when using the large distance of 4m. The incidence angle of the FNG airfoil is held constant at $\alpha = 10°$, which is close to stall. During the upward rotation of the NACA 0021 airfoil a time step size of $\Delta t = 1.5 \cdot 10^{-5}$s is chosen; afterwards it is increased to $\Delta t = 5 \cdot 10^{-5}$s.

In all simulations Re=2.0×10^6 (with respect to c=0.6m) and Ma= 0.15 have been used. At the in- and outflow of the wind tunnel the farfield boundary condition is applied, while at the upper and lower end of the wind tunnel inviscid walls are utilised, thus neglecting the viscous effects of the wind tunnel walls. At the 2 airfoils viscous walls are chosen.

One goal of the computations is to identify the most reliable numerical setting with respect to the turbulence model and the airfoil-to-airfoil distance. This is in particular useful with regard to forthcoming 3D-computations.

The second aim is to check whether the vortex-airfoil interaction has a significant effect on C_l and leads to stall (defined as massive flow separation) at the FNG airfoil.

Figures 7–13 show the vorticity based on the SAO-computations at various times of the simulations, where on the left the small airfoil-to-airfoil distance of 2m is considered, while the figures on the right are based on the large distance of 4m. As the vorticity looks almost identical with Menter-SST, only the SAO-results are shown.

Before switching to dual time stepping, steady restart solutions have been performed at the beginning of all four simulations. Figure 7 shows the vorticity of these solutions on cutouts of the computational domains. Focusing on the area of the vortex generation grid and the vortex transport grid, both results look almost identical. At the right boundary of the vortex transport grid the vorticity vanishes, which is a hint that the background grid is too coarse to conserve it, while both the vortex generation grid and the vortex transport grid are sufficiently fine.

Next the NACA 0021 airfoil is rotated 10° upwards within $1.5 \cdot 10^{-2}s$. The resulting vorticity plots are shown in Fig. 8. In both simulations the vortex has evolved from the trailing edge and has already been interpolated partly onto the vortex transport grid. Furthermore, the vortex has started to split up into several subvortices. This effect is caused by discretisation errors including the ones due to the Chimera interpolation. In physics this phenomenon can also be observed behind an airfoil, where it emerges due to geometrical unevenness.

After $1.9 \cdot 10^{-2} s$ the vortex has been interpolated onto the vortex transport grid, which is shown in Fig. 9. Now the vortex transport grid is transported with the freestream velocity of $50 \frac{m}{s}$ to the right.

At $t = 2.5 \cdot 10^{-2} s$ the vortex transport grid has moved 0.3m towards the FNG airfoil, which is indicated in Fig. 10. The results based on the small and the large airfoil-to-airfoil distance still look identical and the vortex has continued to split into subvortices.

The vortex transport grid is further transported to the right, until it reaches its final position at $t = 3.1 \cdot 10^{-2} s$ in the case of the small airfoil-to-airfoil distance and at $t = 7.1 \cdot 10^{-2} s$ in the large one. At this stage, which is indicated in Fig. 11, the vortex transport grid is stopped, while the vortex continues to move to the right. Due to the longer physical time passed in the simulation using the large airfoil-to-airfoil distance, the vortex has dissipated more than in the case of the small distance.

After $t = 3.9 \cdot 10^{-2} s$ and alternatively $t = 7.9 \cdot 10^{-2} s$ the vortex has been partly interpolated onto the vortex interaction grid, which is shown in Fig. 12. While the vortex in the case of the small airfoil-to-airfoil distance still contains higher maximal vorticity values than in the simulations using a large distance, it has also become weaker. One possible explanation for this relatively fast vortex decay might be, that the vortex is interpolated several times onto different Chimera grids, which adds up the numerical error.

While the simulations were continued for an even longer time, Fig. 13 shows the vorticity plots at $t = 4.7 \cdot 10^{-2} s$ and respectively $t = 8.7 \cdot 10^{-2} s$. In both cases a main vortex has evolved at the right of the longitudinal vortex above the FNG airfoil.

Judging by the vorticity plots, all simulations performed satisfactory, whereas the vortex dissipation seems to be more severe in the case of the large airfoil-to-airfoil distance due to the longer physical time.

Next the effect of the vortex-FNG interaction on C_l is examined. Figure 14 shows the C_l-distributions of all four computations, where in the left picture the curves are based on the two simulations using the small distance, while in Fig. 14 (right) the computations using the large distance are considered. Note the different time scales in both pictures. The following observations can be made:

Firstly, the effect of the vortex-airfoil interaction on C_l is much stronger when using the small distance, independently of the underlying turbulence model. Only in the two computations using the small distance a lift breakdown occurs.

Secondly, both turbulence models result in similar C_l-curves, but the values based on the SAO computations are larger by $\Delta C_l \approx 0.2$.

The final question examined is whether stall occurs due to the vortex-airfoil interaction. This is obviously not the case in the two simulations using the large distance, because no lift breakdown can be observed. As furthermore both turbulence models behave qualitatively similar, it is sufficient to look at the results obtained by SAO in the case of the small airfoil-to-airfoil distance of 2m. (The results of Menter-SST using a small distance were also examined and turned out to be similar to SAO.) Figure 15 and Fig. 16 show C_f at $t = 4.1 \cdot 10^{-2} s$, $t = 4.5 \cdot 10^{-2} s$ and $t = 4.9 \cdot 10^{-2} s$. These are the points in time, when C_l reaches a local minimimum, a local maximum and again a local minimum. The flap remains fully attached in all cases. As additionally also the flow at the main wing does not detach, it is hereby proven that in this computation no stall occurs.

4 Conclusion

A Chimera technique for moving grids was used to simulate the generation and transport of large-scale vortices and to model their interaction with a two-element airfoil near stall. The method requires three fine Chimera grids - one that includes the airfoil to generate the vortex, one grid to transport the vortex and one grid that resolves the airfoil, which in the end interacts with the vortex. The background grid covering most of the computational domain can be chosen relatively coarse, which minimes the numerical costs.

For the results shown in section 3 a NACA 0021 airfoil was used to generate the vortex, while the airfoil interacting with the vortex was an FNG-airfoil at $\alpha = 10°$. As both two different turbulent models - SAO and Menter-SST - and two airfoil-to-airfoil distances of 2m and alternatively 4m were used, an overall of four simulations have been performed. While in all computations the vortex was successfully generated, transported and interacted with the FNG airfoil, only in the two simulations using the small airfoil-to-airfoil distance a breakdown of C_l could be observed at the FNG airfoil due to the vortex-airfoil interaction. Nevertheless in none of the four simulations stall occured at the FNG airfoil. Regarding the variation of the turbulence models, both models behaved qualitatively similar, i.e. they resulted in similar C_l-curves, but the values based on the SAO computations were larger by $\Delta C_l \approx 0.2$.

For future work, it is planned to perform 3D-computations using either URANS, LES or DES methods. Based on the results shown in this publication, a small airfoil-to-airfoil distance of 2m is preferred over a large distance of 4m. Although only two-dimensional results have been shown in this publication, the proposed Chimera method can be directly applied to three-dimensional problems.

Acknowledgments

References

[1] de Bruin, A. C., "Wake Vortex Evolution and ENcounter (WAVENC)," *Air and Space Europe*, Vol. 2, No. 5, pp. 84-87, September 2000.

[2] Holzäpfel, F., "Probabilistic Two–Phase Aircraft Wake–Vortex Model: Furter Development and Assessment," *Journal of Aircraft*, Vol. 43, No. 3, pp. 700–708, 2006.

[3] Cerretelli, C. and Williamson, C. H. K., "The Physical Mechanism of Vortex Merging," *Journal of Fluid Mechanics*, Vol. 475, pp. 41-77, 2003.

[4] Abate, M., "Gust Boundary Condition for the TAU-Code," Technical Report IB 124–2007/9, DLR, Braunschweig, Germany, November 2007.

[5] Ren, T. and Edwards, J. A., "Vortex Interaction with an Aerofoil Using Chimera and the AMR algorithm," *AIAA Atmospheric Flight Mechanics Conference and Exhibit*, AIAA 2002-4806, Monterey, Californa, 5-8 August 2002.

[6] Xu, H., Khalid, M., and Mamou, M., "Investigation of Flows Past Mult-Element Airfoils using Chimera Grid and Quasi–Steady Approach," 2nd Interantional Bhurban Conference on Applied Sciences and Technology, Bhurban, Pakistan, June 16–21, 2003.

[7] Schwamborn, D., Gerhold, T., and Heinrich, R., "The DLR Tau-Code: Recent Applications in Research and Industry," ECCOMAS CFD 2006, edited by Wesseling, P, Onate, E. and Periaux, J., Technical University Delft, The Netherlands, 2006.

[8] Mavriplis, D. J., Jameson, A., and Martinelli, L., "Multigrid Solution of the Navier-Stokes Equations on Triangular Meshes," Technical Report, ICASE-report No. 89-35, 1989.

[9] Dwight, R., "Time-Accurate Navier-Stokes Calculations with Approximately Factored Implicit Schemes," *Computational Fluid Dynamics 2004*, edited by Groth, C. and Zingg, D.W., Springer, 2004, pp. 211–218.

[10] Schwarz, T., "Ein blockstrukturiertes Verfahren zur Simulation der Umströmung komplexer Konfigurationen," DLR-Forschungsbericht 2005-20, 122 p., ISSN 1434–8454, 2005.

[11] Cho, K. W., Kwon, J. H., and Lee, S., "Development of a Fully Systemized Chimera Methodology for Steady/Unsteady Problems," *Journal of Aircraft*, Vol. 36, No. 6, pp. 973–980, 1999.

[12] Petersson, N. A., "Hole–Cutting for Three–Dimensional Overlapping Grids," *SIAM Journal on Scientific Computing*, Society for Industrial and Applied Mathematics, Vol. 21, No. 2, pp. 646–665, 1999.

[13] Wu, Z.–N., "Uniqueness of Steady–State Solutions for Difference Equations on Overlapping Grids," *SIAM Journal on Numerical Analysis*, Vol. 33, No. 4, pp. 1336–1357, 1996.

[14] Chesshire, G. and Henshaw, W. D., "Composite Overlapping Meshes for the Solution of Partial Differential Equations," *Journal of Computational Physics*, Vol. 90, pp. 1–64, 1990.

[15] Holst, T. L, "Chimera Donor Cell Search Algorithm Suitable for Solving the Full Potential Equation," *Journal of Aircraft*, Vol. 37, No. 1, pp. 76–84, 2000.
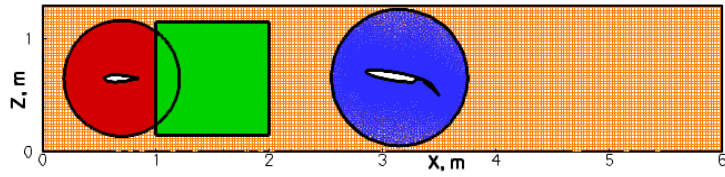
Figure 1: Relative position of the four Chimera grids at the beginning of the computation.
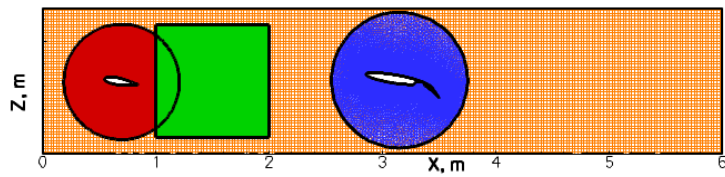
Figure 2: Relative position of the four Chimera grids after the red "vortex generation grid" has been flapped upwards.
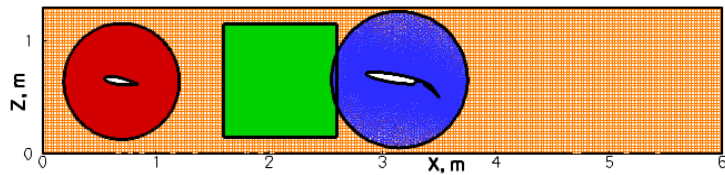

Figure 3: Relative position of the four Chimera grids after the green "vortex transport grid" has been stopped.
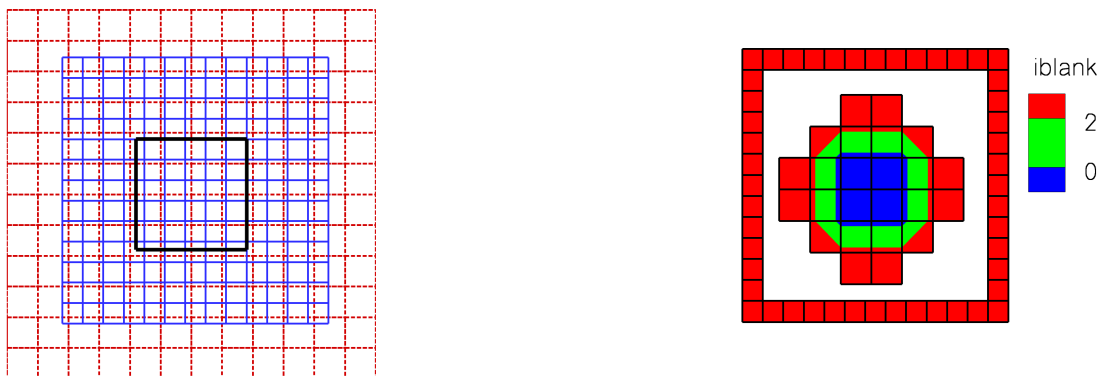

Figure 4: Vortex grid (solid blue lines) and boundary of a hole definition grid (solid black lines) placed within a background grid (dashed red lines) (left) and corresponding grid points with iblank values 0 or 2 (right)
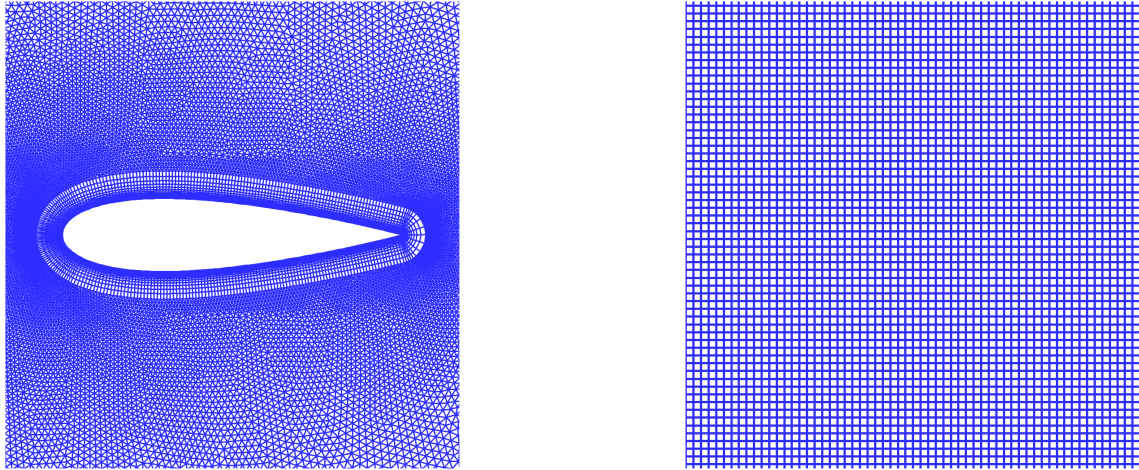
Figure 5: Cutout of size $0.4m \times 0.4m$ of vortex generation grid (left) and of vortex transport grid (right).
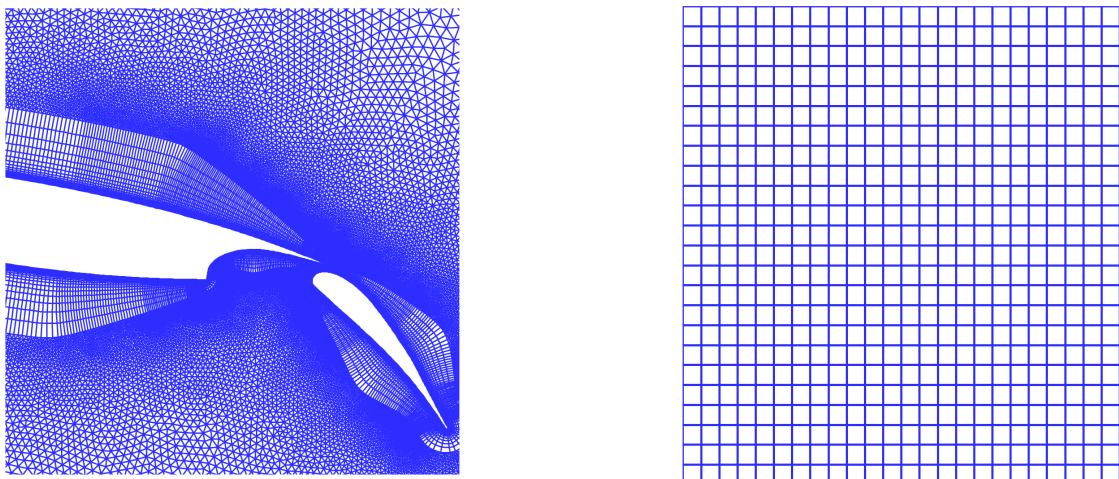
Figure 6: Cutout of size $0.4m \times 0.4m$ of vortex interaction grid (left) and of background grid (right).
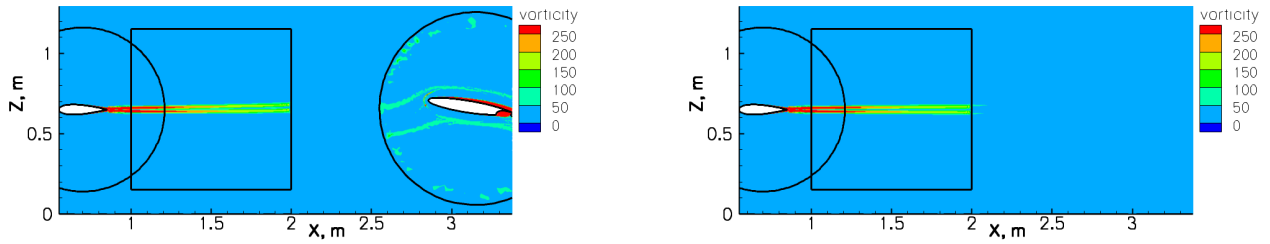
Figure 7: Vorticity based on SAO computations at $t = 0s$ using the small airfoil-to-airfoil distance of 2m (left) and the large airfoil-to-airfoil distance of 4m (right).
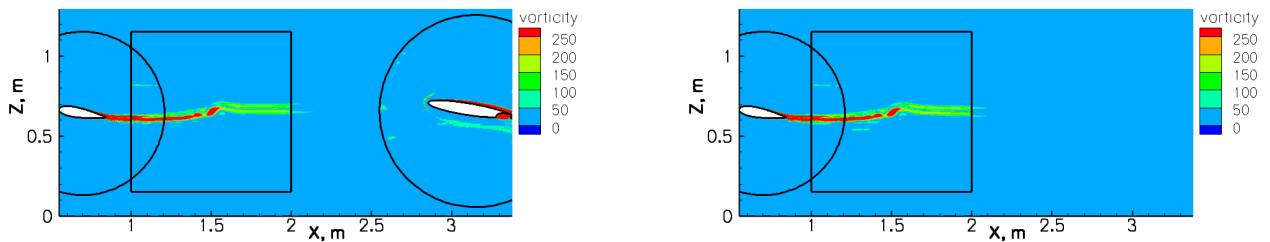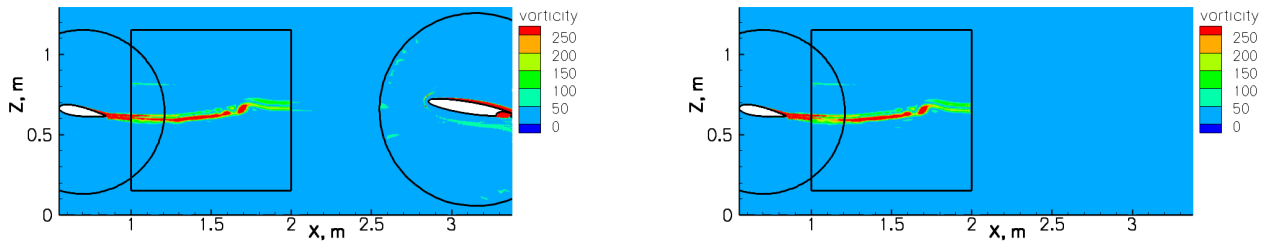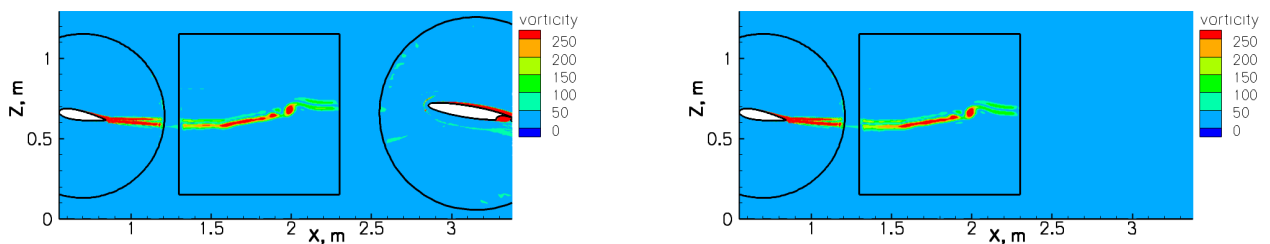

Figure 8: Vorticity based on SAO computations at $t = 1.5 \cdot 10^{-2}s$ using the small airfoil-to-airfoil distance of 2m (left) and the large airfoil-to-airfoil distance of 4m (right).
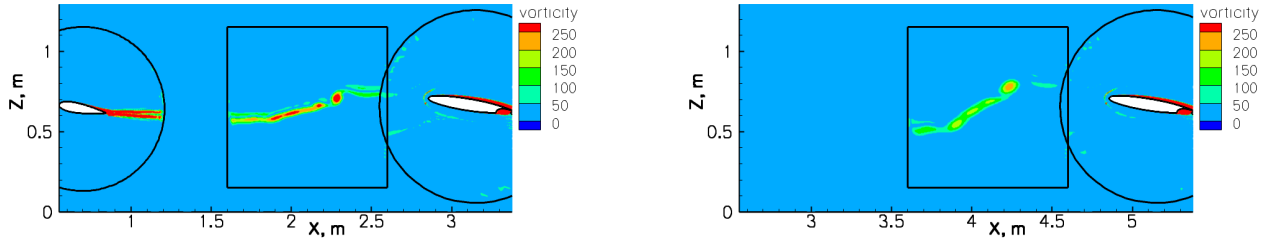

Figure 9: Vorticity based on SAO computations at $t = 1.9 \cdot 10^{-2}s$ using the small airfoil-to-airfoil distance of 2m (left) and the large airfoil-to-airfoil distance of 4m (right).

Figure 10: Vorticity based on SAO computations at $t = 2.5 \cdot 10^{-2}s$ using the small airfoil-to-airfoil distance of 2m (left) and the large airfoil-to-airfoil distance of 4m (right).

Figure 11: Vorticity based on SAO computations at $t = 3.1 \cdot 10^{-2} s$ using the small airfoil-to-airfoil distance of 2m (left) and at $t = 7.1 \cdot 10^{-2} s$ using the large airfoil-to-airfoil distance of 4m (right).
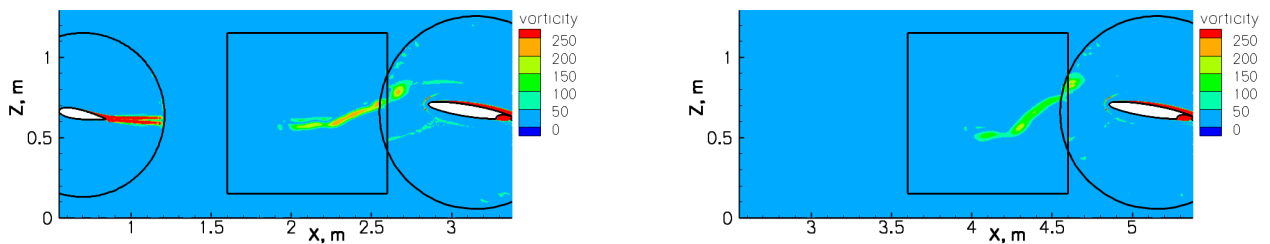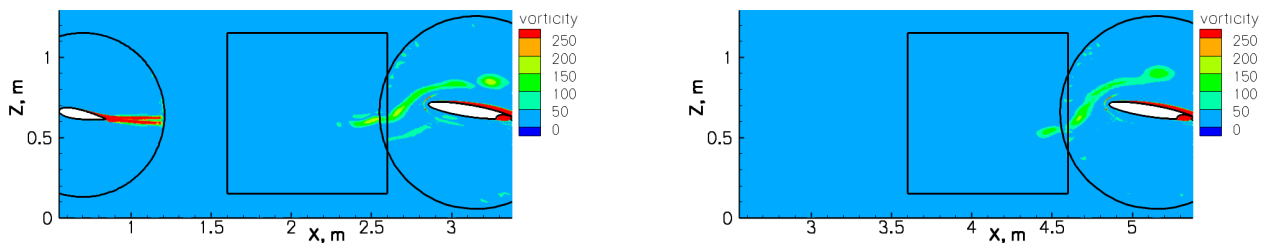

Figure 12: Vorticity based on SAO computations at $t = 3.9 \cdot 10^{-2} s$ using the small airfoil-to-airfoil distance of 2m (left) and at $t = 7.9 \cdot 10^{-2} s$ using the large airfoil-to-airfoil distance of 4m (right).

Figure 13: Vorticity based on SAO computations at $t = 4.7 \cdot 10^{-2} s$ using the small airfoil-to-airfoil distance of 2m (left) and at $t = 8.7 \cdot 10^{-2} s$ using the large airfoil-to-airfoil distance of 4m (right).
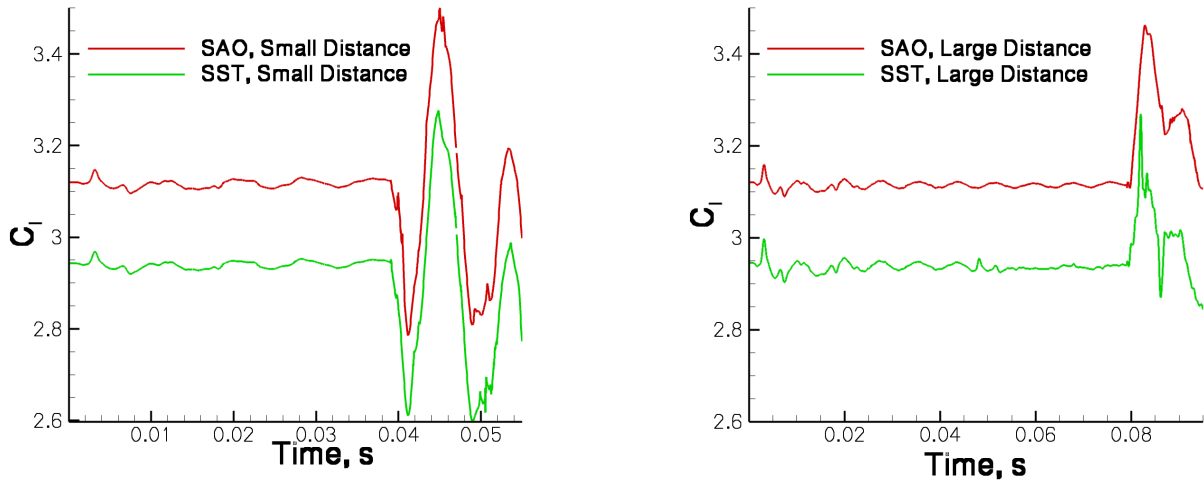
Figure 14: Time-dependent lift coefficients based on the SAO and Menter-SST models when using the small airfoil-to-airfoil distance of 2m (left) and the large airfoil-to-airfoil distance of 4m (right).
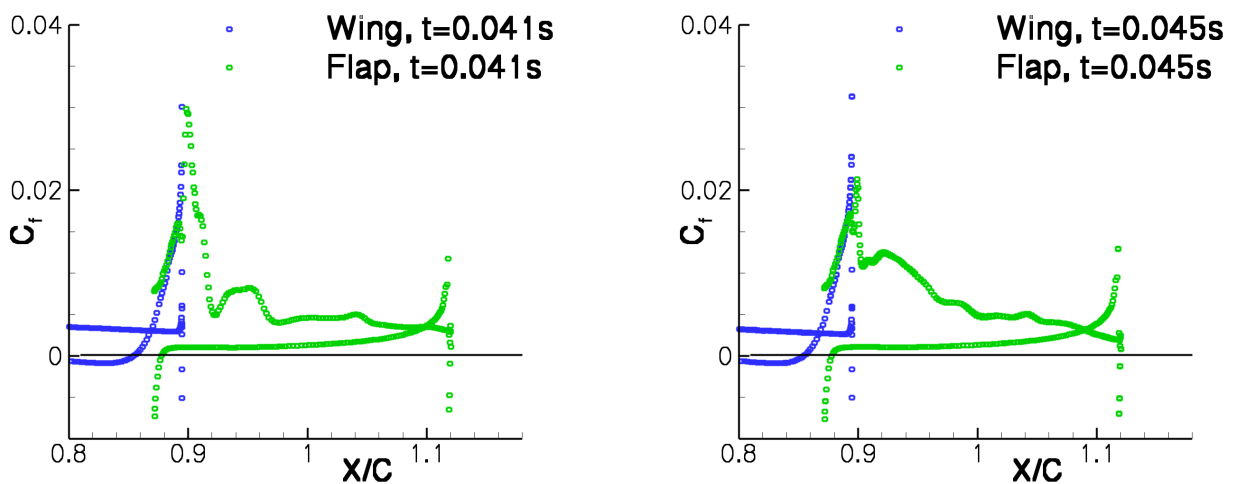

Figure 15: Skin friction coefficients based on the SAO computation using the small airfoil-to-airfoil distance of 2m at $t = 4.1 \cdot 10^{-2}s$ (left) and $t = 4.5 \cdot 10^{-2}s$ (right).
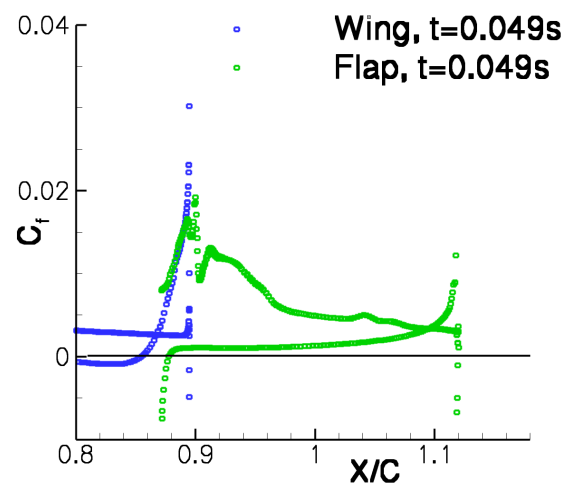
Figure 16: Skin friction coefficients based on the SAO computation using the small airfoil-to-airfoil distance of 2m at $t = 4.9 \cdot 10^{-2}s$.